ACS NANO

www.acsnano.org

ARTICLE

Precursor-Confined Chemical Vapor Deposition of 2D Single-Crystalline Se_xTe_{1-x} Nanosheets for p-Type Transistors and Inverters

Haoxin Huang,[¶] Jiajia Zha,[¶] Songcen Xu, Peng Yang,* Yunpeng Xia, Huide Wang, Dechen Dong, Long Zheng, Yao Yao, Yuxuan Zhang, Ye Chen, Johnny C. Ho, Hau Ping Chan, Chunsong Zhao,* and Chaoliang Tan*

Cite This: *ACS Nano* 2024, 18, 17293−17303

Read Online

ACCESS | Metrics & More | Article Recommendations | Supporting Information

ABSTRACT: Two-dimensional (2D) tellurium (Te) is emerging as a promising p-type candidate for constructing complementary metal-oxide-semiconductor (CMOS) architectures. However, its small bandgap leads to a high leakage current and a low on/off current ratio. Although alloying Te with selenium (Se) can tune its bandgap, thermally evaporated Se_xTe_{1-x} thin films often suffer from grain boundaries and high-density defects. Herein, we introduce a precursor-confined chemical vapor deposition (CVD) method for synthesizing single-crystalline Se_xTe_{1-x} alloy nanosheets. These nanosheets, with tunable compositions, are ideal for high-performance field-effect transistors (FETs) and 2D inverters. The preformation of Se−Te frameworks in our developed CVD method plays a critical role in the growth of Se_xTe_{1-x} nanosheets with high crystallinity. Optimizing the Se composition resulted in a $Se_{0.30}Te_{0.70}$ nanosheet-based p-type FET with a large on/off current ratio of 4×10^5 and a room-temperature hole mobility of 120 $cm^2 \cdot V^{-1} \cdot s^{-1}$, being eight times higher than thermally evaporated Se_xTe_{1-x} with similar composition and thickness. Moreover, we successfully fabricated an inverter based on p-type $Se_{0.30}Te_{0.70}$ and n-type MoS_2 nanosheets, demonstrating a typical voltage transfer curve with a gain of 30 at an operation voltage of V_{dd} = 3 V.

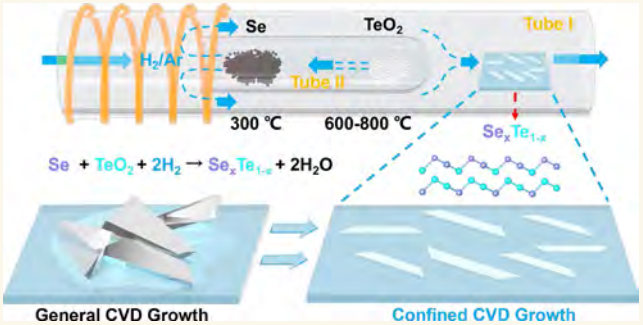

KEYWORDS: *precursor-confined, chemical vapor deposition, Se_xTe_{1-x} nanosheets, 2D transistors, inverters*

INTRODUCTION

Silicon (Si)-based complementary metal-oxide-semiconductor (CMOS) architecture, featuring low power consumption, wide working voltage range, and strong anti-interference ability, plays an indispensable role in today's high-performance central processing unit (CPU) chips.[1−3] However, it is a daunting challenge to improve the density of Si transistors since its further scaling is limited by the short channel effect.[2] An alternative strategy is to develop multilevel circuits in the back-end-of-line (BEOL) process, and the emerging two-dimensional (2D) materials are promising candidates.[4,5] 2D materials exhibit an atomically thin nature with self-passivated surfaces, making them suitable for multilayer integration. Researchers have already demonstrated that constructing CMOS circuits based on n- and p-type 2D semiconductors could facilitate the realization of monolithic three-dimensional integrated circuits (3D-ICs).[2,6−8] On the other hand, compared with various n-type semiconductors showing competitive carrier transport behaviors with Si, such as thin film oxides (e.g., IGZO and ZnO),[9,10] 2D transition-metal dichalcogenides (TMDs, e.g., MoS_2 and WS_2),[11] and monochalcogenides (e.g., InSe),[6] high-performance p-type counterparts remain to be further explored.[1,12−16] Although several 2D semiconductors such as WSe_2 could be applied to construct p-type metal-oxide-

Received: April 22, 2024
Revised: May 28, 2024
Accepted: June 5, 2024
Published: June 17, 2024

https://doi.org/10.1021/acsnano.4c05323
ACS Nano 2024, 18, 17293−17303

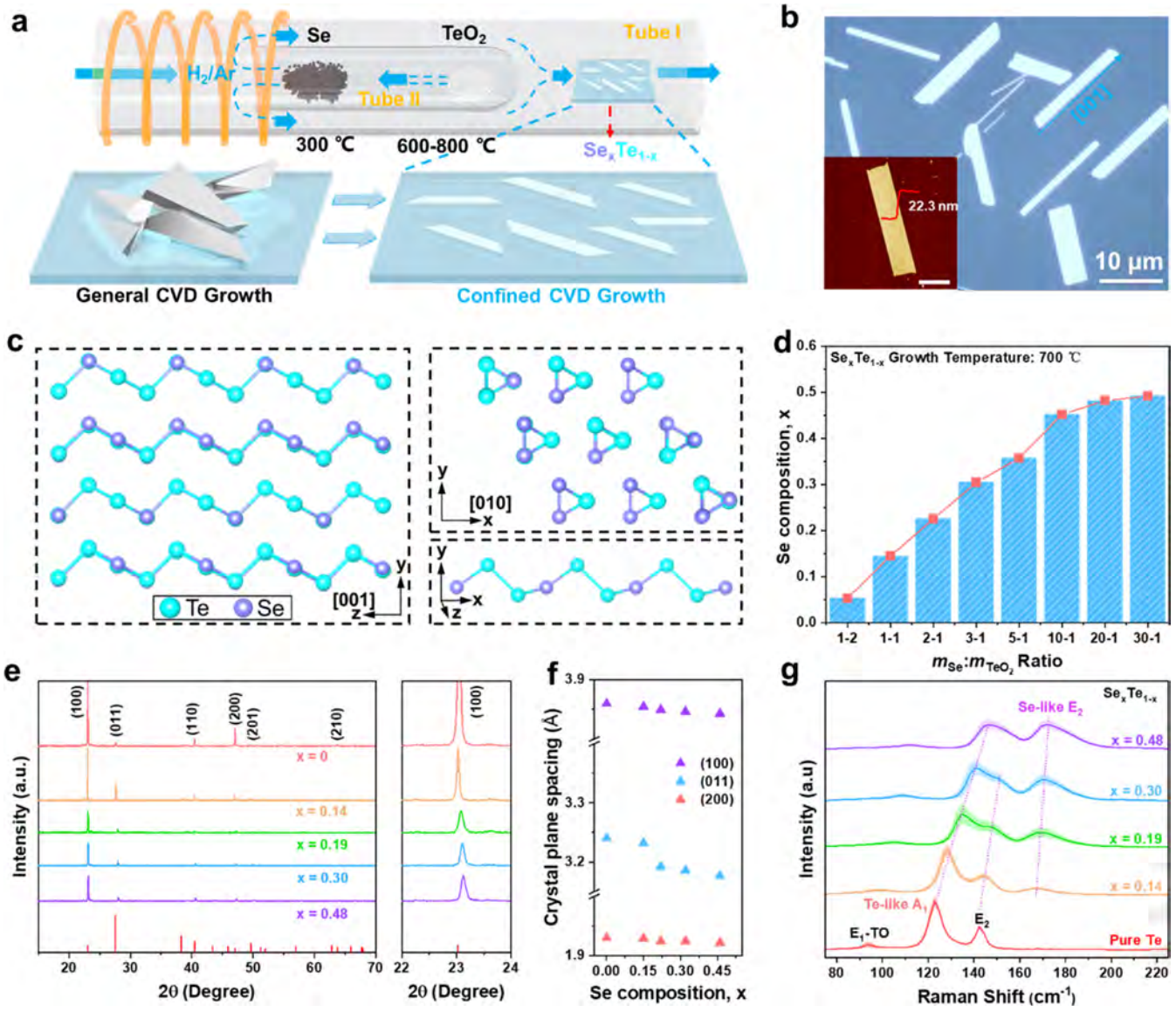

Figure 1. Growth and characterization of single-crystalline Se_xTe_{1-x} alloy nanosheets. (a) Schematic illustration of the CVD growth of Se_xTe_{1-x} nanosheets enabled by confining precursors within the partially open tubes to create a reverse flow of vapor mixture. The bottom panels compare the products grown using the standard CVD method and the confined CVD method. (b) Optical image of representative Se_xTe_{1-x} alloy nanosheets epitaxially grown on mica. Inset: AFM profile of a selected nanosheet with a thickness of 22.3 nm (scale bar: 3 μm). (c) Crystal structure of Se_xTe_{1-x} alloy shown in different views. (d) Histogram showing the Se composition (x) varied as a function of precursor-ratio in single-crystalline alloy nanosheets (growth temperature: 700 °C). (e) Full-range XRD patterns of Se_xTe_{1-x} alloys recorded with different Se compositions (x increases from 0 to 0.48). (f) Variation trend of the crystal plane spacing d of (100), (011), and (200) crystal planes. (g) Raman patterns of Se_xTe_{1-x} alloy nanosheets with Se composition increasing from 0 to 0.48.

semiconductor (p-MOS),[13,14] its performance has been severely impeded by the considerable contact resistance.

Recently, 2D p-type elemental semiconductors have emerged as ideal candidates as they usually hold a small effective mass of holes, m_h^*,[13,14] one of which has been extensively studied is black phosphorus (bP), and bP-based field-effect transistor (FET) exhibits field-effect hole mobility (μ_{FE}) of ~1000 $cm^2 \cdot V^{-1} \cdot s^{-1}$.[17] Unfortunately, further application of bP nanosheets has been impeded by their fast degradation under ambient conditions. The recently rediscovered van der Waals (vdW) elemental tellurium (Te) could be another alternative, which is composed of one-dimensional (1D) helical chains hexagonally stacked with each other via vdW force.[1,18] The wide spectrum of intriguing properties, including thickness-dependent bandgap, high room-temperature hole mobilities (>1000 $cm^2 \cdot V^{-1} \cdot s^{-1}$), and superior mechanical and thermoelectric properties guarantee its application prospect in advanced electronics and optoelectronics.[1,19−21] The reported Te FETs based on hydrothermal-synthesized Te nanoflake exhibit comparable electronic performance with bP FET but without a noticeable performance degradation after being exposed in the air for over 2 months.[18] However, hydrothermal methods usually introduce additional surface contamination, and the nanosheet agglomeration phenomenon also hinders its scale production. On the other hand, chemical vapor deposition (CVD) is widely used for preparing high-quality 2D crystals.[22] Ultrathin vertically grown crystalline Te nanoflake has been reported by Zhang et

https://doi.org/10.1021/acsnano.4c05323
ACS Nano 2024, 18, 17293−17303

al., while the corresponding FET shows unsatisfactory on-state current and weak electrostatic regulation.[23] Yang et al. then reported the CVD growth of Te nanobelts along its *c*-axis on atomically flat hexagonal boron nitride (h-BN) for Te FET with high room-temperature hole mobility up to 1370 $cm^2 \cdot V^{-1} \cdot s^{-1}$.[24] However, the recorded moderate on/off current ratios (~10 to 10^2) limit their applications in subsequent logic circuits. Alloying Te with another chalcogen Se has been demonstrated as an effective method to tune the bandgap of Se_xTe_{1-x} alloy from Te (0.3 eV) to Se (1.8 eV) for better device performance.[19,25−27] In 2020, Tan et al. reported the thermally evaporated Se_xTe_{1-x} thin films for high-performance short-wave infrared (SWIR) photoconductors and a focal plane array.[19] After the optimization of Se composition to 0.32, the fabricated devices present a good trade-off between on/off current ratios and Hall mobilities. Recently, evaporated Se-alloyed Te-TeO_x film was reported by Liu et al., which showed improved on/off current ratios with moderate mobilities (~15 $cm^2 \cdot V^{-1} \cdot s^{-1}$).[28] However, the hole mobility values are still much less than those of p-type Si transistors.

In this work, we report high-quality single-crystalline Se_xTe_{1-x} alloy nanosheets with tunable compositions prepared via a precursor-confined CVD method for high-performance p-type FET and CMOS inverter. The single-crystalline nature of Se_xTe_{1-x} nanosheets is clearly identified by high-resolution transmission electron microscopy (HRTEM) results. The premixing of the precursor in the confining space leads to the successful growth of 2D Se_xTe_{1-x} alloy in our designed CVD process. The Se composition of the alloy can be continuously tuned from 0 to 0.49. We further characterized the composition-dependent electrical properties of Se_xTe_{1-x} nanosheets and determined the optimized Se composition. The high-performance p-type FET based on $Se_{0.30}Te_{0.70}$ nanosheet achieves a decent on/off current ratio of 4×10^5 and high room-temperature hole mobility of 120 $cm^2 \cdot V^{-1} \cdot s^{-1}$, which is competitive among the existing 2D elemental material-based FETs (refer to Table S1). We further demonstrate its application potential in logic circuits by constructing a CMOS inverter by integrating it with the MoS_2 channel, which achieves a high gain of ~30 at V_{dd} = 3 V.

RESULTS AND DISCUSSION

Growth and Characterization of Single-Crystalline Se_xTe_{1-x} Nanosheets. Quartz tubes (I and II) loaded in the two-zone atmospheric-pressure CVD system (Figure 1a) were used for the synthesis of Se_xTe_{1-x} alloy nanosheets (see the Experimental Section). Specifically, a partially open quartz tube II placed in the quartz tube I was incorporated to accommodate the two precursor materials (Se and tellurium oxide (TeO_2)), which will be evaporated at 300 and 600−800 °C, respectively, and then reduced by H_2/Ar carrier gas to produce vapor mixture. The growth of Se_xTe_{1-x} alloys presents a morphology transition from 1D to 2D with the increase of the evaporation temperature of TeO_2 (Figure S1), which can be attributed to the increased lateral and longitudinal atomic migration speed.[29−31] In particular, when the temperature is below ~600 °C, our products tend to grow into 1D morphology (Figure S1(a)). When the temperature reaches 800 °C, these single-crystalline Se_xTe_{1-x} nanosheets would agglomerate into large clusters (Figure S1(c)). Thus, we kept the evaporation temperature of the precursors at 700 °C to obtain 2D Se_xTe_{1-x} alloy nanosheets. Notably, the special placement of quartz tube II creates extra confined space that allows the reverse flow of reactive vapors and enables thorough mixing and prereaction during the gas feeding process. Subsequently, these premixed Se/Te vapor mixtures will grow into Se_xTe_{1-x} alloy nanosheets onto the mica substrate via vdW epitaxy.[30] While the absence of confined premixing typically results in the growth of bulk/thick crystals, as depicted in Figure 1a and the optical images shown in Figure S2(a−f). The distinct product morphology can be explained by the weak absorption energy of Se compared to Te atoms on mica. Our preliminary experiments (Figure S3(a,b)) have revealed that the Se species show a high tendency to epitaxially grow on the surface of crystalline Te nanosheets, as reported by other literature.[29,32] Subsequent observations (Figure S3(c,d)) indicate that the sole Se precursor only leads to the growth of irregular Se particles on mica. Therefore, we can conclude that Te plays a critical role as the structural framework in the growth of the Se_xTe_{1-x} alloy, and insufficient mixing of the precursors may result in excessive nucleation of Se on the Te surface or competitive adsorption with Te on the substrate surface, undermining the framework formation.

Thus, our simple design effectively suppresses the epitaxial process of Se atoms and ensures the mixture of the gas precursors for the stable growth kinetics of the Se_xTe_{1-x} alloy. The growth mechanism is depicted as follows: The confined space guarantees the prior incorporation of Se atoms into the Te lattice/anchor on Te chains rather than the surface epitaxy during the reduction process (Figure S2(a−d)), thus leading to a stable reactive vapor and, ultimately, the formation of single-crystalline Se_xTe_{1-x} alloy nanosheets (Figure S2(f)). In a typical chemical reaction (eq 1), TeO_2 undergoes partial reduction by H_2 gas, yielding volatile Te/Te−O species.[23,24] Simultaneously, due to the structural similarity between Se and Te crystals, Se seamlessly substitutes partial Te atoms in the helical chains. The precursor material is then transported downstream via carrier gas and deposited onto mica substrate, ultimately diffusing and rearranging into a well-aligned alloy layer:

$$2H_2 + Se + TeO_2 \rightarrow Se_xTe_{1-x} + 2H_2O \quad (1)$$

Figure 1b depicts the typical optical microscopy (OM) images of Se_xTe_{1-x} (x = ~ 0.3) alloy nanosheets, most of which exhibit a trapezoidal structure like Te with lateral and longitudinal dimensions ranging from 1 to 5 μm and 5 to over 10 μm, respectively. The embedded atomic force microscopy (AFM) topography reveals a typical alloyed nanosheet thickness of 22.3 nm, and the minimum thickness can reach about 10 nm (Figure S4 for detailed information). The schematic structure of the Se_xTe_{1-x} is then shown in Figure 1c, exhibiting a basic 1D helical chain structure.[15,19,33] Since they have similar crystal structures, Se atoms can partially substitute for Te atoms, and then, Se/Te atoms form covalent bonds with neighboring atoms to maintain the material stability. Specifically, the atomic chains of Se/Te twist into a triangular shape (viewed from the *z*-direction) and then interact with other chains through vdW forces, resulting in a hexagonal array structure.[19,34]

The Se_xTe_{1-x} alloy nanosheets with different chemical compositions (x = 0−0.49) are realized by controlling the mass ratio of Se powders and TeO_2 powders at separated temperature zones (Figure 1d), which was characterized by transmission electron microscopy accompanied by energy-dispersive spectroscopy (TEM-EDS) (Figure S5 for detailed information). Notably, the composition of Se in the alloy does

https://doi.org/10.1021/acsnano.4c05323
ACS Nano 2024, 18, 17293−17303

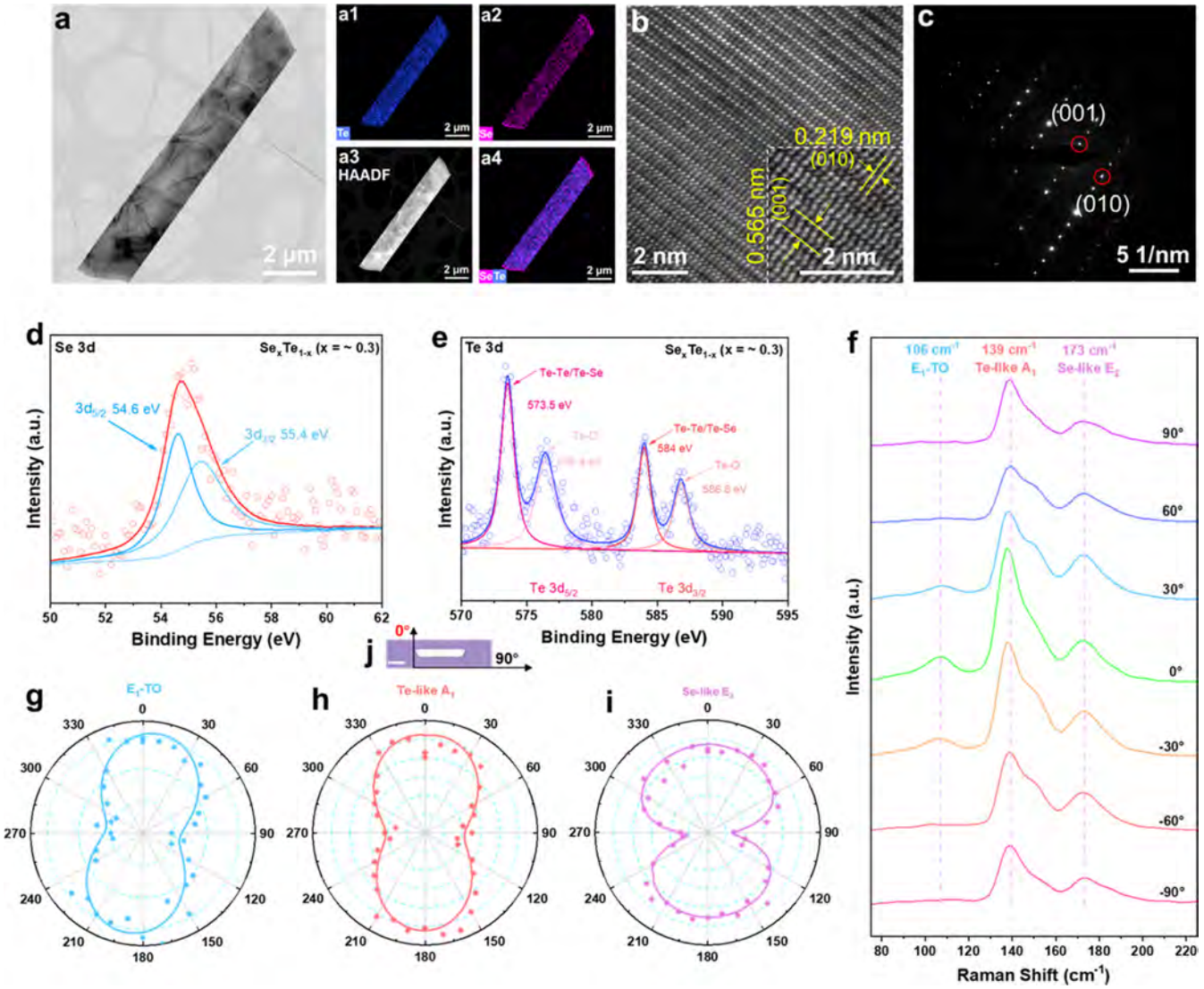

Figure 2. Characterization of single-crystalline $Se_{0.3}Te_{0.7}$ nanosheets. (a) TEM image of a selected $Se_{0.3}Te_{0.7}$ nanosheet and the corresponding elemental mappings: (a1) mapping of Te element, (a2) mapping of Se element, (a3) HAADF-STEM image of $Se_{0.3}Te_{0.7}$ nanosheet, (a4) combined mapping of both Se and Te elements. (b) HRTEM image of the selected $Se_{0.3}Te_{0.7}$ nanosheet with the inset clearly revealing the chain structure of the alloy nanosheet. (c) SAED pattern of $Se_{0.3}Te_{0.7}$ nanosheet. (d) Se 3d XPS peaks and (e) Te 3d XPS peaks with fitted characteristic peaks. (f) Angle-resolved polarized Raman results of $Se_{0.3}Te_{0.7}$ nanosheet in typical angles and fitted polar figures of Raman intensity corresponding to (g) E_1-TO, (h) Te-like A_1, and (i) Se-like E_2 modes located at 106, 139, and 173 cm^{-1}, respectively. (j) Illustration of the rotation angle in angle-resolved polarized Raman characterization.

not exhibit a linear relationship with the weight ratio of precursors, and the critical value (x) is approximately 0.5. According to Figure S6, the distribution density of CVD-grown alloy nanosheets decreases with the Se:TeO_2 weight ratio. When the weight ratio is less than 30, the products mainly maintain the morphology of thin nanosheets (Figure S6(a,b)). On the other hand, with further increasing the precursor weight ratio, the products tend to grow into thick nanosheets and thorny clusters (Figure S6(c)). This phenomenon can be explained by the low nucleation energy of Se on the mica surface, which is insufficient to support the epitaxy growth under higher vapor pressure.[35,36] The excess Se vapor will grow and aggregate with Te at the nucleation points, thereby hindering the formation of 2D nanosheets. This result confirms the critical role of Te in framework formation during diffusion growth. To characterize the crystal quality of our CVD-synthesized Se_xTe_{1-x} alloy nanosheets, X-ray diffraction (XRD) characterization was further employed. As shown in Figure 1e, the full-range XRD patterns of the synthesized Se_xTe_{1-x} nanosheets (x = 0–0.48) show distinct characteristic peaks, where the peaks of the Te (x = 0) (a = b = 4.456 Å and c = 5.921 Å) match well with the reference value of PDF#97–006–5692 (P3121 space group).[18,20,34] It can be observed that the (100) crystal plane exhibits the highest strength, which corroborates the diffusion growth of the alloy along the [001] crystal direction rather than vertical growth.[18,35,37] The interplanar crystal spacing d of the (100), (011), and (200) peaks at 2θ = 22.96–23.13, 27.66–28.02, and 47.08–47.25° were plotted as a function of x (Figure 1f) to uncover the variation tendency. The diffraction angles of selected peaks gradually increase with Se composition, manifesting the decrease of lattice constants.[25,38] That originates from the smaller atomic radius of the Se atom compared with that of the Te atom (1.17 and 1.42 Å, respectively). The compositional

https://doi.org/10.1021/acsnano.4c05323
ACS Nano 2024, 18, 17293–17303

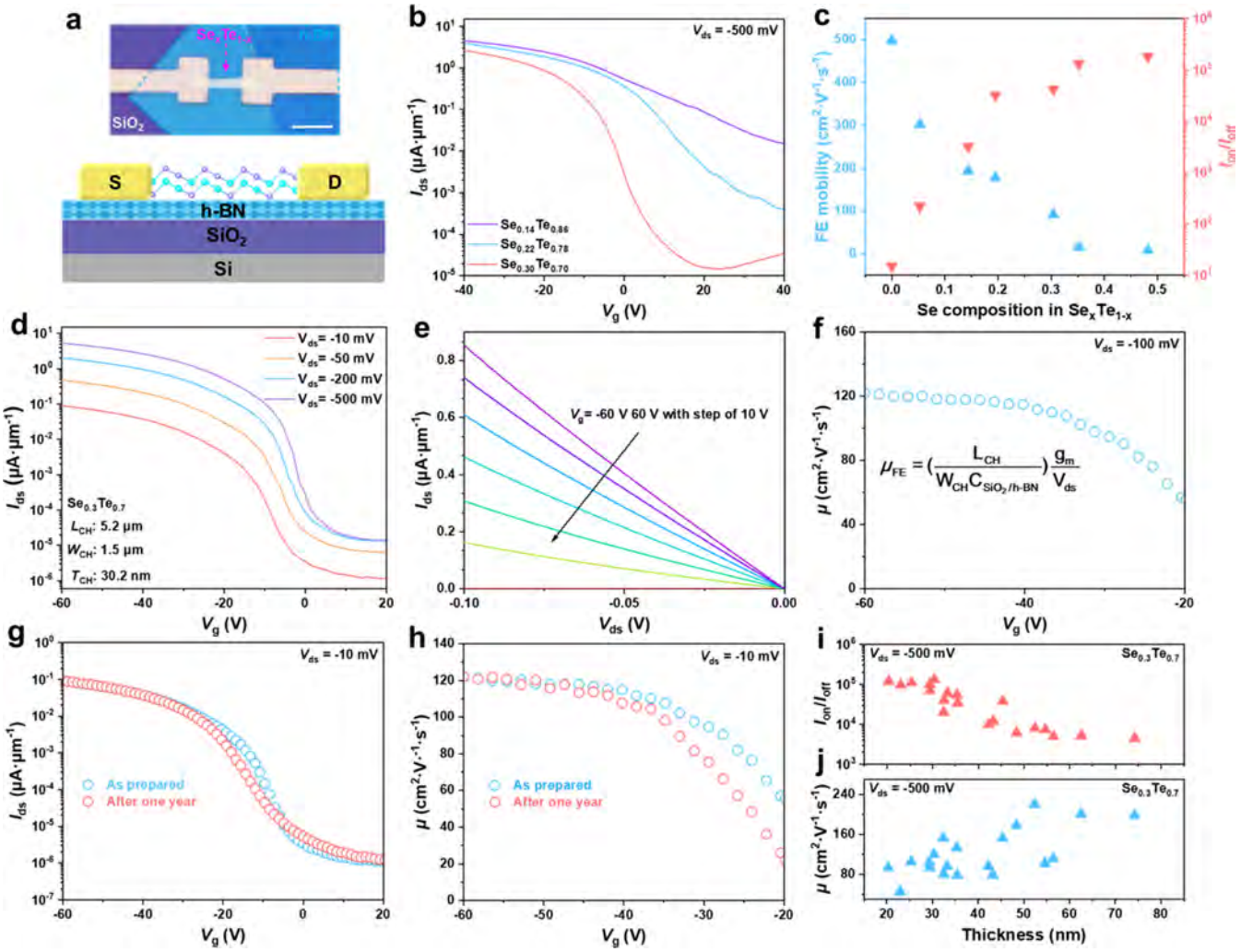

Figure 3. Electrical performance of FETs based on Se_xTe_{1-x} alloy nanosheets. (a) Schematic illustration and optical image of Se_xTe_{1-x} FET. (scale bar: 10 μm). (b) Transfer curves of FETs based on Se_xTe_{1-x} nanosheets with different Se composition (x = 0.14, 0.22, and 0.30). The used Se_xTe_{1-x} nanosheets have similar morphology. (c) Se composition-dependent field-effect mobilities and on/off current ratios. (d) Transfer curves of a typical $Se_{0.3}Te_{0.7}$ FET with L_{CH} of 5.2 μm, W_{CH} of 1.5 μm, and T_{CH} of 30.2 nm, respectively. (e) Output curves of a typical $Se_{0.3}Te_{0.7}$ FET with V_g varying from −60 to 60 V in a step of 10 V. (f) Extracted back gate voltage-dependent field-effect mobilities. (g) Transfer curves and (h) extracted field-effect mobilities of the typical device when tested as prepared and exposed in air for over one year. Statistic performance summary of the (i) on/off current ratios and (j) field-effect mobilities obtained from 20 $Se_{0.3}Te_{0.7}$ FETs with increased channel thickness.

uniformity and transition of the synthesized nanosheets can be further characterized by Raman spectroscopy. As depicted in Figure 1g, it is evident that randomly selected 20 Se_xTe_{1-x} alloy nanosheets with different compositions exhibit similar characteristic peak positions. Characteristic peaks of Te (x = 0) are located at 93.6, 122.8, and 142.3 cm^{-1}, corresponding to the E_1-TO, A_1 (Te-like), and E_2 modes, respectively.[18,19] With the increase of Se composition, Te-like A_1 and E_2 modes gradually shift to greater wavenumbers and merge into a broad peak. Meanwhile, the Se-like E_2 mode begins to emerge at a moderate Se composition of x = ∼ 14%. As the Se composition further increases, the peak intensity ratio between Se-like E_2 mode and A_1 mode also increases gradually (characteristic peaks for pure crystalline Se: 144.06 cm^{-1} (E_1), 232.95 cm^{-1} (E_2), and 236.83 cm^{-1} (A_1), Figure S7), indicating the well-grown alloy nanosheets with high crystallinity.

Detailed Characterization of $Se_{0.3}Te_{0.7}$ Nanosheets. As indicated by our electronic characterization of Se_xTe_{1-x} alloy nanosheets, the Se composition of ∼0.3 exhibits the best trade-off between the on/off current ratios and hole mobilities, which will be discussed later. In this context, we further analyze the atomic structural morphology and quality of the prepared $Se_{0.3}Te_{0.7}$ alloy nanosheets by high-angle annular dark-field scanning transmission electron microscopy (HAADF-STEM), HRTEM, and energy-dispersive X-ray spectroscopy (EDS). The Se_xTe_{1-x} nanosheet with an average Se composition of ∼0.3 was confirmed via EDS elemental analysis (Figure S5(b)). As shown in Figure 2a1−a4, the EDS mapping results clearly demonstrate the uniform distribution of Se and Te elements throughout the nanosheet. It should be noted that Se atoms exhibit a pronounced tendency to aggregate at the longitudinal terminal, attributing to the existence of dangling bonds at molecular chain terminals that are common in 1D materials.[19] Figure 2b depicts a typical atomic HRTEM image of $Se_{0.3}Te_{0.7}$ with discernible helical chains, which exhibit a 3-fold screw symmetry along [001]. The interplanar distances of the (001) and (010) crystallographic planes are calculated to be 2.19 and 5.6 Å, respectively. These values are smaller than

https://doi.org/10.1021/acsnano.4c05323
ACS Nano 2024, 18, 17293−17303

the corresponding crystal planes of elemental Te crystal (2.2 and 6.0 Å, respectively) due to the partial substitution of Se atoms with a smaller atomic radius.[18] This observation consists well with the results obtained from XRD. Additionally, Figures 2c and S8 illustrate the alloy nanosheet's selected area electron diffraction (SAED) patterns obtained from different locations, revealing distinct lattice points and rotationally symmetric spots with the same crystallographic zone axis. The HRTEM images and SAED patterns confirm the single-crystalline nature of the synthesized alloy nanosheets with the primary growth direction along the [001] crystallographic axis.

The elemental composition and chemical states of the single-crystalline alloys were further uncovered by X-ray photoelectron spectroscopy (XPS). Although within the same batch of samples, the Se composition in the XPS-tested sample ($x \sim 0.33$) is slightly higher than that for TEM analysis ($x \sim 0.30$), possibly due to the absorption of amorphous Se on the mica surface. The XPS peaks of Se 3d located at 55.4 and 54.6 eV shown in Figure 2d are fitted based on the principle of spin−orbit splitting into Se $3d_{3/2}$ and Se $3d_{5/2}$ binding energy, respectively. This result suggests the moderate reduction state of Se in the alloy configuration, as Se^{2-} is expected $3d_{5/2}$ to be lower than 55.0 eV, which can be attributed to the greater electronegativity of Se atoms in comparison to Te atoms.[35,39] The fitted Te 3d XPS graph is shown in Figure 2e, with two characteristic peaks located at 573.5 and 584.0 eV corresponding to Te $3d_{5/2}$ and Te $3d_{3/2}$ orbits of the Te bonded to Se,[40,41] respectively. It is worth pointing out that the satellite peaks related to the oxidation state of Te^{4+} also appear, commonly observed among ultrathin Te nanoflakes/films under moderate annealing and originate from the inevitable baking process in our experimental process. It is noted that the surface oxidation can be well removed via pre-etching before XPS, leaving the characteristic peaks unchanged (refer to Figure S9). We further explored the anisotropic optical properties of our CVD-synthesized $Se_{0.3}Te_{0.7}$ sample with moderate thicknesses by angle-resolved polarized Raman spectroscopy. Nanosheet samples were first transferred onto SiO_2/Si substrate (see Figure S10). As shown in Figure 2f, periodic variations in the intensity of characteristic Raman peaks are observed through the automatic rotation of a half-wave plate at a step of 30°. The polarization started from the direction perpendicular (i.e., 0°) to the *c*-axis of the nanosheet (i.e., [001]), as shown in Figure 2j. By refining the rotation angle to 10°, the peak intensities corresponding to different modes present noticeable periodic changes with the rotation angles. We then plotted these into the polar figures, which also fit with the Sine/Lorentz function for better visualization (Figure 2g−i). It is clear that the intensity variation of E_1-TO and Te-like A_1 modes are similar to that of elemental Te crystal, with the maximum values obtained at the polarization direction perpendicular to the *c*-axis (i.e., 0 and 180°). This result further confirms the preference growth of Se_xTe_{1-x} alloy in the [001] crystal direction, consistent with the HRTEM figure. Meanwhile, the Se-like E_2 vibration mode is significantly affected by the alloyed Se atoms. This manifests in the reduction of symmetry in the polar coordinate, transitioning from double-symmetry axes to a single-symmetry axis,[24,42] while the maximum values occur at around ∼45°.

Electrical Performance of Se_xTe_{1-x}-Based FET. Previous research has demonstrated that Se_xTe_{1-x} alloys hold great promise as the potential p-type semiconductor channel.[19,43] However, the application potential of transistors based on Se_xTe_{1-x} prepared previously has not been entirely squeezed out due to the unsatisfactory crystal quality. Leveraging the high crystallinity of our CVD-synthesized Se_xTe_{1-x} alloy nanosheets, we constructed back-gated FETs based on Se_xTe_{1-x} via a dry transfer method.[44] In addition, we employed surface-passivated h-BN nanosheets to reduce interface scattering and traps.[24,45] The schematic diagram of the Se_xTe_{1-x}/h-BN-based FET is depicted in Figure 3a, with Au (∼40 nm) as contact metal and a heavily doped Si as the back gate which is covered by 300 nm SiO_2 serving as the gate dielectric. The transfer characteristics of Se_xTe_{1-x} transistors with varied Se compositions are depicted in Figure 3b, employing a sweeping range from −40 to +40 V. Notably, as the Se composition increases, the on/off current ratio of the measured transistor significantly improves from 10^2 to 10^5. In contrast, the on-state current density decreases by less than one order of magnitude. We also statistically analyzed the alloy-composition-dependent hole mobilities and on/off current ratios, as shown in Figure 3c. It can be concluded that the Se_xTe_{1-x} FET has the best trade-off between the on/off current ratios and hole mobilities at a Se composition of ∼0.3.

Based on the above analysis, we selected $Se_{0.3}Te_{0.7}$ alloy nanosheets as the channel material for constructing high-performance p-type FET. The thickness of the typical nanosheet is 30.2 nm (refer to Figure S11(a−e) for the AFM profiles of the selected device). The device's transfer curves are shown in Figure 3d with typical p-type transport characteristics. The energy band diagram of $Se_{0.3}Te_{0.7}$ FET under ON and OFF states are further depicted in Figure S11(f,g), respectively. After applying the negative back gate voltage, holes will accumulate in the channel and result in a small resistance, while under the positive back gate voltage, holes will be depleted and result in a large resistance. Under different biases (−10, −50, −200, −500 mV), the obtained transfer curves exhibit an on/off current ratio exceeding 10^5, and the gate leakage current (I_{gs}) recorded (refer to Figure S12) is as low as ∼1 to 10 pA, manifesting the good stability of gate dielectrics. It is worth mentioning that when the channel bias is −500 mV, the $Se_{0.3}Te_{0.7}$ FET achieves an impressive on/off current ratio of 4×10^5 as well as an on-state current approaching 10 $\mu A \cdot \mu m^{-1}$. This encouraging electronic performance of the $Se_{0.3}Te_{0.7}$ FET can be explained through bandgap engineering. Te thin films are difficult to be electronically depleted due to their extremely narrow bandgap (approximately 0.3 eV).[1,15,19] However, after alloying with Se, the bandgap of Te can be effectively tuned. In addition, the high crystal quality enables simultaneous strong light absorption and low dark current, thus holding great potential for constructing advanced electronics and optoelectronics in the future.[1,19,43,46] The contact quality in the device can be discerned from the output characteristics. As shown in Figure 3e, the channel current linearly increases with the absolute value of the bias voltage under different gate voltages, indicating the realization of good contact between the Au electrodes and the $Se_{0.3}Te_{0.7}$ channel. We further extracted the contact resistance using the TLM (transmission line method),[47] which tells a decent contact resistance value of R_c = 3250 Ω·μm (Figure S13). The field-effect mobility (μ_{FE}) can be estimated via eq 2:[48]

https://doi.org/10.1021/acsnano.4c05323
ACS Nano 2024, 18, 17293−17303

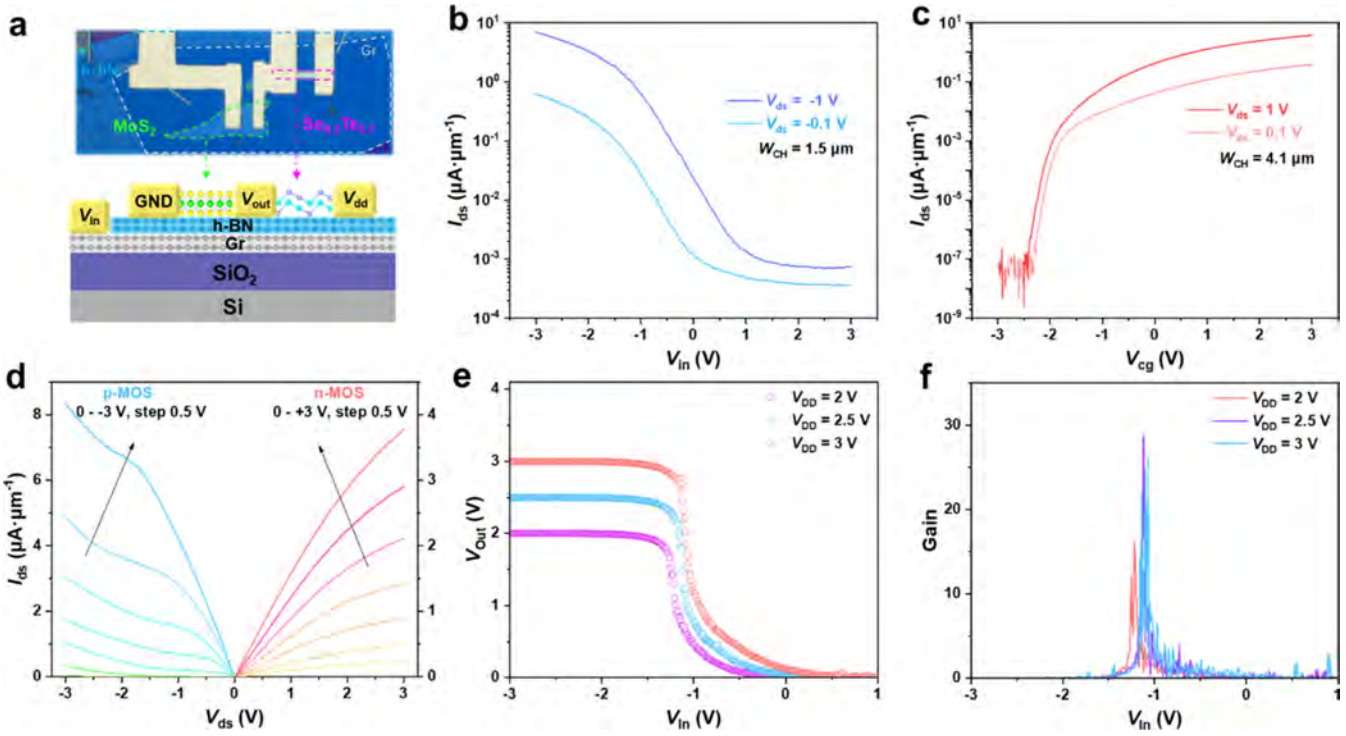

Figure 4. Performance characterization of 2D inverter based on $Se_{0.3}Te_{0.7}$ and MoS_2 nanosheets. (a) Optical image and schematic illustration of the 2D inverter based on p-type $Se_{0.3}Te_{0.7}$ and n-type MoS_2 FETs. Transfer curves of (b) p-FET and (c) n-FET tested at different V_{ds}. (d) Comparison of the output curves of p-type FET (blue line) and n-type FET (red line). (e) Voltage transfer curves (VTCs) of 2D inverter at different V_{dd} of 2, 2.5, and 3 V, respectively. (f) Extracted voltage gain (G) from VTCs indicates the voltage gain ($=-d(V_{out})/d(V_{in})$) of the inverter reaches 30 at V_{dd} = 3 V.

$$\mu_{FE} = \left(\frac{L_{CH}}{W_{CH}C_{SiO_2/h\text{-}BN}}\right)\frac{g_m}{V_{ds}} \quad (2)$$

where L_{CH} and W_{CH} represent the channel length and width, respectively; $C_{SiO_2/h\text{-}BN}$ is the capacitance of the SiO_2/h-BN dielectric, which is estimated to be 12.0 nF·cm^{-2}; and g_m refers to the transconductance in the transfer curves and is expressed as $d(I_{ds})/d(V_{gs})$. At V_{ds} = −0.1 V, the peak field-effect hole mobility of the $Se_{0.3}Te_{0.7}$ FET is calculated to be 120 cm^2·V^{-1}·s^{-1} (Figure 3f). Furthermore, we have also revealed the excellent air stability of the alloy-based transistor. We retested the electrical property of the $Se_{0.3}Te_{0.7}$-based transistor after being exposed to air for over one year, and the results are presented in Figure 3g,h. Moreover, without deliberate encapsulation, the Se_xTe_{1-x} FET with a channel thickness of 30.2 nm did not show significant performance degradation, and the observed slight threshold voltage (V_{th}) shift could be explained by molecular (e.g., H_2O) adsorption. In addition, we further measured 20 different Se_xTe_{1-x} FETs fabricated on h-BN/SiO_2/Si and bare SiO_2/Si substrates, respectively (representative samples are shown in Figure S15), where two key figures of merit are recorded (the on/off current ratios and the field-effect hole mobilities). The nanosheet thickness ranged from 20 to 75 nm. According to Figure S15, it can be observed that even without the insertion of h-BN nanoflakes, transistors can still exhibit excellent performance, indicating the high quality of the CVD-synthesized Se_xTe_{1-x} nanosheets. As shown in Figure 3i,j, the field-effect hole mobilities of $Se_{0.3}Te_{0.7}$ FETs exhibit a gradual increase with thicker channels (from ∼50 cm^2·V^{-1}·s^{-1} to greater than 200 cm^2·V^{-1}·s^{-1}), while the on/off current ratios decreased from 10^5 to 10^3. These thickness-dependent transport behaviors are quite common for layered materials and are often attributed to interlayer coupling and screening effects.[17,49] Overall, compared to physical vapor deposition (PVD)-prepared polycrystalline $Se_{0.32}Te_{0.68}$ thin films, our CVD-synthesized single-crystalline $Se_{0.3}Te_{0.7}$ nanosheets show a seven to eight times increase in the hole mobility and a two order of magnitude improvement in the on/off current ratio (see Table S1 for more details). These enhancements can be attributed to eliminated grain boundaries and significantly reduced defect density, which reduces scattering and local stress,[50] ultimately enhancing hole transport behaviors. Although Se_xTe_{1-x} alloy nanosheets show inferior hole mobilities compared to Te nanocrystals, it is still competitive or even superior to n-type 2D semiconductors such as MoS_2. Moreover, the good performance trade-off between the carrier mobilities and on/off current ratios will promote its development in fabricating high-performance electronics and optoelectronics.[19,43]

CMOS Inverter Based on p-Type $Se_{0.3}Te_{0.7}$ and n-Type MoS_2. Considering that our prepared $Se_{0.3}Te_{0.7}$ alloy nanosheets exhibit competitive performance to their n-type counterparts such as MoS_2, we further constructed a 2D CMOS inverter based on p-type $Se_{0.3}Te_{0.7}$ and n-type MoS_2 nanosheets. Figure 4a shows the optical image and schematic illustration of the 2D inverter in the local bottom gate architecture residing on SiO_2 (300 nm)/Si substrate, and the thickness profiles of the components are shown in Figure S14. The inverter fabrication starts from the exfoliation and transfer of atomically thin h-BN and graphene (Gr) nanoflakes onto the Si/SiO_2 substrate, which function as the dielectric layer and local bottom gate, respectively, for better gate control and steeper subthreshold swing (SS). Then, the selected $Se_{0.3}Te_{0.7}$

https://doi.org/10.1021/acsnano.4c05323
ACS Nano 2024, 18, 17293−17303

and MoS_2 nanosheets were transferred onto the h-BN/Gr heterostructure, followed by the deposition of Au as the electrodes in different functional areas (see the Experimental Section for details). Figure 4b depicts the typical transfer curves of the individual $Se_{0.3}Te_{0.7}$ FET within the inverter, showing an on-state current >7 $\mu A{\cdot}\mu m^{-1}$ and an on/off current ratio of $\sim 10^4$ at $V_{ds} = -1$ V. Such a performance matches well with our previous results, indicating the high repeatability of our synthesis method, and the relatively small on/off current ratio can be explained by the unavoidable variation in sheet thickness during growth. Meanwhile, $Se_{0.3}Te_{0.7}$ p-MOS also provides a positive threshold voltage (V_{th}) that is closer to 0 (0.2 V for $V_{dd} = -0.1$ and 0.6 V for $V_{dd} = -1$ V), thus creating a suitable switching interval during the operation of the designed inverter. Compared with the MoS_2 FET, the $Se_{0.3}Te_{0.7}$ FET shows a diminished gate control capacity at higher bias with increased V_{th}. This drain-induced barrier lowering (DIBL) phenomenon can also be observed in other 2D alloy-based FETs, which can be attributed to the strengthened alloying scattering under higher bias.[51,52] The MoS_2 n-MOS (Figure 4c) shows an admiring on/off current ratio of $\sim 10^6$ and the on-state current reaches 3 $\mu A{\cdot}\mu m^{-1}$. However, the extracted V_{th} of −2.4 V is far from the zero point, which may originate from the sulfur vacancies introduced in the mechanical exfoliation and is expected to be amended via further annealing.[53,54] Figure 4d compares the output curves of $Se_{0.3}Te_{0.7}$ and MoS_2 FETs under V_g ranging from 0 to −3 V and 0 to +3 V in a step of 0.5 V, respectively. The p- and n-type devices have nearly symmetric $I_{ds}-V_{ds}$ characteristics. It is noted that the output curves of $Se_{0.3}Te_{0.7}$ FET show an obvious up-kick phenomenon, possibly due to the reduction of potential barrier height for electron transport and the kink effect originating from impact ionization at large bias.[1,17,18,55] Figure 4e provides the voltage transfer curves (VTCs) of the 2D inverter with V_{dd} increased from 2 to 3 V when V_{in} sweeping from −3 to 3 V, and the output voltage gradually switches from high to low level. The corresponding voltage gain (G) is then extracted via $-d(V_{out})/d(V_{in})$ and plotted in Figure 4f, showing a peak gain value of ∼30 at $V_{dd} = 3$ V. This considerable static VTC property demonstrated in the 2D inverter fabricated from our synthesized $Se_{0.3}Te_{0.7}$ alloy nanosheet reveals its application potential in advanced logic circuits in the future.

CONCLUSIONS

In summary, we have successfully synthesized high-quality single-crystalline Se_xTe_{1-x} alloy nanosheets via a precursor-confined CVD method and conducted a comprehensive study of their electrical properties. Our findings demonstrated that the improved crystallinity significantly enhances the device performance of FETs based on Se_xTe_{1-x} alloy nanosheets, which mainly includes considerable on/off current ratios and much higher field-effect hole mobilities (e.g., μ_{FE} has been increased by 8-fold compared to the PVD-prepared counterpart). In addition, we successfully fabricated the 2D inverter based on a p-type Se_xTe_{1-x} FET and an n-type MoS_2 FET with a voltage gain of ∼30 at $V_{dd} = 3$ V. The Se_xTe_{1-x} alloy nanosheets may also find promising applications for the fabrication of advanced optoelectronics.

EXPERIMENTAL SECTION

Growth Method of Single-Crystalline Se_xTe_{1-x} Nanosheets. The single-crystalline Se_xTe_{1-x} nanosheets were grown on mica using Se (99.999%, Sigma-Aldrich) and TeO_2 (99.999%, Sigma-Aldrich) powders as precursors via a modified CVD method. Two precursors were placed at opposite ends of a quartz tube (∼20 cm), with the tube opening facing the direction of the carrier gas. Se powder was loaded in the low-temperature evaporation zone (∼300 °C), while TeO_2 powder was loaded in the high-temperature zone (600−800 °C). Additionally, the mica (0.5 cm × 0.5 cm) substrate was placed approximately 15 cm from the quartz tube. Before the reaction, the tube chamber was purged three times with a 10% hydrogen−argon (H_2/Ar) mixture. At the start of the reaction, a 100 sccm flow of 10% H_2/Ar mixture was introduced, functioning as the reaction gas and carrier gas simultaneously, and the whole setup operates at atmospheric pressure. Both temperature zones were raised to the specified temperatures within 30 min. The reaction duration was 30 min, followed by rapid removal of the quartz tube from the heating zone to achieve rapid cooling and suppress excessive epitaxial growth of nanosheets on the mica substrate.

Materials Characterizations. The morphologies of the Se_xTe_{1-x} nanosheets were characterized by optical microscopy (Nikon, ECLIPSE LV100ND). The surface morphologies and height profiles of the Se_xTe_{1-x} alloy nanosheets were measured by AFM (Bruker, Dimension Icon with Scan Asyst). The Raman spectra were measured by Renishaw with a polarized incident laser tuned via a half-wave plate (the incident polarized light and the exiting polarized light are parallel in orientation) at room temperature; the wavelength of the excitation laser is 532 nm. HRTEM and SAED images were obtained by Tecnai F20 TEM (TF20). XPS (Thermo Scientific K-α) analysis was performed using an Al X-ray source with a diameter beam spot of 400 μm. The X-ray diffraction patterns were obtained from Rigaku SmartLab using Cu−Kα radiation under a working voltage of 30 kV.

Device Fabrication. The Se_xTe_{1-x} back-gated FETs on SiO_2 (300 nm)/Si or h-BN/SiO_2 (300 nm)/Si substrate were prepared via the standard electron-beam lithography (EBL) technique (TESCAN, VEGA3) followed by the deposition of Au (40 nm) as source/drain electrodes. First, the h-BN nanoflakes were exfoliated onto SiO_2/Si from the bulk crystal using poly(dimethylsiloxane) (PDMS). Then, the Se_xTe_{1-x} alloy nanosheets will be transferred onto the as-prepared h-BN nanosheets via the poly(methyl methacrylate) (PMMA)-assisted dry transfer method. Similarly, the fabrication of a 2D inverter started from the exfoliation of graphene (Gr) and h-BN nanoflakes, which will be stacked into the h-BN/Gr heterostructure by the PDMS-stamp above method. Bulk h-BN, MoS_2, and graphite single crystals were purchased from the 2D semiconductors. Subsequently, the selected Se_xTe_{1-x} and exfoliated MoS_2 nanosheets will be aligned and released to the required position using a high-precision platform, followed by the standard EBL and deposition of contact metal (Au with a thickness of ∼40 nm) to fabricate the electrodes corresponding to input (V_{in}), output (V_{out}), and drain/source (V_{dd}/GND) electrodes.

Electrical Measurement. All of the measurements of the device characteristics were performed in the dark under ambient conditions using a semiconductor parameter analyzer (HP4155C, Agilent Technologies).

ASSOCIATED CONTENT

Supporting Information

The Supporting Information is available free of charge at https://pubs.acs.org/doi/10.1021/acsnano.4c05323.

Optical images of Se_xTe_{1-x} alloy nanosheets prepared under different temperatures; comparison between normal CVD growth and precursor-confined CVD growth of alloy nanosheets; growth of Se on pure Te nanosheets and bare mica substrate; AFM profiles of additional alloy nanosheets; TEM-EDS analysis results of alloy nanosheets with different composition (x); optical images of alloy nanosheets synthesized with different precursor weight ratios; Raman characterization of pure Se nanosheet; additional SAED patterns of

https://doi.org/10.1021/acsnano.4c05323
ACS Nano 2024, 18, 17293−17303

$Se_{0.3}Te_{0.7}$ alloy nanosheets; XPS analysis of alloy nanosheets tested after pre-etching; optical images of alloy nanosheets on SiO_2/Si substrate; AFM profiles of selected $Se_{0.3}Te_{0.7}$ alloy nanosheet-based FET and the band diagram during working; gate leakage current of alloy-based FET during test; contact resistance test of alloy-based FET; AFM profiles of different components used in the alloy-based inverter; and transfer curves of representative $Se_{0.3}Te_{0.7}$ FETs prepared on different substrates (PDF)

AUTHOR INFORMATION

Corresponding Authors

Peng Yang − *College of Integrated Circuits and Optoelectronic Chips, Shenzhen Technology University, Shenzhen 518118, China*; Email: yangpeng@sztu.edu.cn

Chunsong Zhao − *Huawei Technologies Co., LTD., Shenzhen 518129, China*; Email: zhaochunsong@hisilicon.com

Chaoliang Tan − *Department of Electrical and Electronic Engineering, University of Hong Kong, Hong Kong SAR, China*; orcid.org/0000-0003-1695-5285; Email: cltan@hku.hk

Authors

Haoxin Huang − *Department of Electrical Engineering, City University of Hong Kong, Hong Kong SAR, China*

Jiajia Zha − *Department of Electrical and Electronic Engineering, University of Hong Kong, Hong Kong SAR, China*

Songcen Xu − *Department of Electronic & Computer Engineering, The Hong Kong University of Science and Technology, Hong Kong SAR, China*

Yunpeng Xia − *Department of Electrical Engineering, City University of Hong Kong, Hong Kong SAR, China*

Huide Wang − *College of Physics and Optoelectronic Engineering, Shenzhen University, Shenzhen 518060, China*

Dechen Dong − *Department of Electrical and Electronic Engineering, University of Hong Kong, Hong Kong SAR, China*

Long Zheng − *Department of Chemistry, The Chinese University of Hong Kong, Hong Kong SAR, China*

Yao Yao − *Department of Chemistry, City University of Hong Kong, Hong Kong SAR, China*

Yuxuan Zhang − *Department of Materials Science and Engineering, City University of Hong Kong, Hong Kong SAR, China*

Ye Chen − *Department of Chemistry, The Chinese University of Hong Kong, Hong Kong SAR, China*; orcid.org/0000-0003-0821-7469

Johnny C. Ho − *Department of Materials Science and Engineering, City University of Hong Kong, Hong Kong SAR, China*; orcid.org/0000-0003-3000-8794

Hau Ping Chan − *Department of Electrical Engineering, City University of Hong Kong, Hong Kong SAR, China*

Complete contact information is available at: https://pubs.acs.org/10.1021/acsnano.4c05323

Author Contributions

¶H.H. and J.Z. contributed equally to this work.

Notes

The authors declare no competing financial interest.

ACKNOWLEDGMENTS

C.T. thanks the funding support from the National Natural Science Foundation of China−Excellent Young Scientists Fund (Hong Kong and Macau) (52122002), ECS scheme (21201821), and General Research Fund (11200122) from the Research Grant Council of Hong Kong. P.Y. thanks the Shenzhen Science and Technology Program (20231128102926002). C.Z. declares this as a non-Huawei service achievement.

REFERENCES

(1) Zhao, C.; Tan, C.; Lien, D.-H.; Song, X.; Amani, M.; Hettick, M.; Nyein, H. Y. Y.; Yuan, Z.; Li, L.; Scott, M. C.; Javey, A. Evaporated Tellurium Thin Films for p-Type Field-Effect Transistors and Circuits. *Nat. Nanotechnol.* **2020**, *15*, 53−58.

(2) Liu, Y.; Duan, X.; Shin, H.-J.; Park, S.; Huang, Y.; Duan, X. Promises and Prospects of Two-Dimensional Transistors. *Nature* **2021**, *591*, 43−53.

(3) Iannaccone, G.; Rizzo, T.; Paliy, M.; Strangio, S.*The Case for Hybrid Analog Neuromorphic Chips Based on Silicon and 2D Materials*, International Electron Devices Meeting (IEDM), 2023; pp 1−4.

(4) Liu, A.; Zhang, X.; Liu, Z.; Li, Y.; Peng, X.; Li, X.; Qin, Y.; Hu, C.; Qiu, Y.; Jiang, H.; Wang, Y.; Li, Y.; Tang, J.; Liu, J.; Guo, H.; Deng, T.; Peng, S.; Tian, H.; Ren, T.-L. The Roadmap of 2D Materials and Devices Toward Chips. *Nano-Micro Lett.* **2024**, *16*, No. 119, DOI: 10.1007/s40820-023-01273-5.

(5) Jiang, J.; Parto, K.; Cao, W.; Banerjee, K.*Monolithic-3D Integration with 2D Materials: Toward Ultimate Vertically-Scaled 3D-ICs*, IEEE SOI-3D-Subthreshold Microelectronics Technology Unified Conference (S3S), 2018; pp 1−3.

(6) Jiang, J.; Xu, L.; Qiu, C.; Peng, L.-M. Ballistic Two-Dimensional InSe Transistors. *Nature* **2023**, *616*, 470−475.

(7) Jayachandran, D.; Pendurthi, R.; Sadaf, M. U. K.; Sakib, N. U.; Pannone, A.; Chen, C.; Han, Y.; Trainor, N.; Kumari, S.; Mc Knight, T. V.; Redwing, J. M.; Yang, Y.; Das, S. Three-Dimensional Integration of Two-Dimensional Field-Effect Transistors. *Nature* **2024**, *625*, 276−281.

(8) Kang, J.-H.; Shin, H.; Kim, K. S.; Song, M.-K.; Lee, D.; Meng, Y.; Choi, C.; Suh, J. M.; Kim, B. J.; Kim, H.; Hoang, A. T.; Park, B.-I.; Zhou, G.; Sundaram, S.; Vuong, P.; Shin, J.; Choe, J.; Xu, Z.; Younas, R.; Kim, J. S.; et al. Monolithic 3D Integration of 2D Materials-Based Electronics Towards Ultimate Edge Computing Solutions. *Nat. Mater.* **2023**, *22*, 1470−1477.

(9) Zhang, J.; Li, Y.; Zhang, B.; Wang, H.; Xin, Q.; Song, A. Flexible Indium-Gallium-Zinc-Oxide Schottky Diode Operating Beyond 2.45 GHz. *Nat. Commun.* **2015**, *6*, No. 7561, DOI: 10.1038/ncomms8561.

(10) Wang, W.; Li, K.; Lan, J.; Shen, M.; Wang, Z.; Feng, X.; Yu, H.; Chen, K.; Li, J.; Zhou, F.; Lin, L.; Zhang, P.; Li, Y. CMOS Backend-of-Line Compatible Memory Array and Logic Circuitries Enabled by High Performance Atomic Layer Deposited ZnO Thin-Film Transistor. *Nat. Commun.* **2023**, *14*, No. 6079, DOI: 10.1038/s41467-023-41868-5.

(11) Sebastian, A.; Pendurthi, R.; Choudhury, T. H.; Redwing, J. M.; Das, S. Benchmarking Monolayer MoS_2 and WS_2 Field-Effect Transistors. *Nat. Commun.* **2021**, *12*, No. 693, DOI: 10.1038/s41467-020-20732-w.

(12) Wu, F.; Tian, H.; Shen, Y.; Hou, Z.; Ren, J.; Gou, G.; Sun, Y.; Yang, Y.; Ren, T.-L. Vertical MoS_2 Transistors with Sub-1-nm Gate Lengths. *Nature* **2022**, *603*, 259−264.

(13) Xiong, Y.; Xu, D.; Feng, Y.; Zhang, G.; Lin, P.; Chen, X. P-Type 2D Semiconductors for Future Electronics. *Adv. Mater.* **2023**, *35*, No. 2206939, DOI: 10.1002/adma.202206939.

(14) He, Q.; Liu, Y.; Tan, C.; Zhai, W.; Nam, G.-h.; Zhang, H. Quest for p-Type Two-dimensional Semiconductors. *ACS Nano* **2019**, *13*, 12294−12300.

(15) Zhao, C.; Batiz, H.; Yasar, B.; Kim, H.; Ji, W.; Scott, M. C.; Chrzan, D. C.; Javey, A. Tellurium Single-Crystal Arrays by Low-

temperature Evaporation and Crystallization. *Adv. Mater.* **2021**, *33*, No. 2100860, DOI: 10.1002/adma.202100860.
(16) Yu, M.; Tan, C.; Gao, X.; Tang, J.; Peng, H. Chemical Vapor Deposition Growth of High-Mobility 2D Semiconductor Bi_2O_2Se: Controllability and Material Quality. *Acta Phys.-Chim. Sin.* **2023**, *39*, No. 2306043, DOI: 10.3866/PKU.WHXB202306043.
(17) Li, L.; Yu, Y.; Ye, G. J.; Ge, Q.; Ou, X.; Wu, H.; Feng, D.; Chen, X. H.; Zhang, Y. Black Phosphorus Field-Effect Transistors. *Nat. Nanotechnol.* **2014**, *9*, 372−377.
(18) Wang, Y.; Qiu, G.; Wang, R.; Huang, S.; Wang, Q.; Liu, Y.; Du, Y.; Goddard, W. A.; Kim, M. J.; Xu, X.; Ye, P. D.; Wu, W. Field-Effect Transistors Made From Solution-Grown Two-Dimensional Tellurene. *Nat. Electron.* **2018**, *1*, 228−236.
(19) Tan, C.; Amani, M.; Zhao, C.; Hettick, M.; Song, X.; Lien, D.-H.; Li, H.; Yeh, M.; Shrestha, V. R.; Crozier, K. B.; Scott, M. C.; Javey, A. Evaporated Se_xTe_{1-x} Thin Films with Tunable Bandgaps for Short-Wave Infrared Photodetectors. *Adv. Mater.* **2020**, *32*, No. 2001329, DOI: 10.1002/adma.202001329.
(20) Amani, M.; Tan, C.; Zhang, G.; Zhao, C.; Bullock, J.; Song, X.; Kim, H.; Shrestha, V. R.; Gao, Y.; Crozier, K. B.; Scott, M.; Javey, A. Solution-Synthesized High-Mobility Tellurium Nanoflakes for Short-Wave Infrared Photodetectors. *ACS Nano* **2018**, *12*, 7253−7263.
(21) Zhang, P.; Liang, Q.; Zhou, Q.; Chen, J.; Li, M.; Deng, Y.; Liang, W.; Zhang, L.; Zhang, Q.; Gu, L.; Ge, C.; Jin, K.-j.; Zhang, C.; Yang, G. High-Performance Terahertz Modulators Induced by Substrate Field in Te-based All-2D Heterojunctions. *Light: Sci. Appl.* **2024**, *13*, No. 67, DOI: 10.1038/s41377-024-01393-6.
(22) Tang, L.; Tan, J.; Nong, H.; Liu, B.; Cheng, H.-M. Chemical Vapor Deposition Growth of Two-Dimensional Compound Materials: Controllability, Material Quality, and Growth Mechanism. *Acc. Mater. Res.* **2021**, *2*, 36−47.
(23) Zhang, X.; Jiang, J.; Suleiman, A. A.; Jin, B.; Hu, X.; Zhou, X.; Zhai, T. Hydrogen-Assisted Growth of Ultrathin Te Flakes with Giant Gate-Dependent Photoresponse. *Adv. Funct. Mater.* **2019**, *29*, No. 1906585, DOI: 10.1002/adfm.201906585.
(24) Yang, P.; Zha, J.; Gao, G.; Zheng, L.; Huang, H.; Xia, Y.; Xu, S.; Xiong, T.; Zhang, Z.; Yang, Z.; Chen, Y.; Ki, D.-K.; Liou, J. J.; Liao, W.; Tan, C. Growth of Tellurium Nanobelts on h-BN for p-Type Transistors with Ultrahigh Hole Mobility. *Nano-Micro Lett.* **2022**, *14*, No. 109, DOI: 10.1007/s40820-022-00852-2.
(25) Li, X.; Long, H.; Zhong, J.; Ding, F.; Li, W.; Zhang, Z.; Song, R.; Huang, W.; Liang, J.; Liu, J.; Wu, R.; Li, B.; Zhao, B.; Yang, X.; Zhang, Z.; Liu, Y.; Wei, Z.; Li, J.; Duan, X. Two-Dimensional Metallic Alloy Contacts with Composition-Tunable Work Functions. *Nat. Electron.* **2023**, *6*, 842−851.
(26) Huang, H.; Zha, J.; Li, S.; Tan, C. Two-Dimensional Alloyed Transition Metal Dichalcogenide Nanosheets: Synthesis and Applications. *Chin. Chem. Lett.* **2022**, *33*, 163−176.
(27) Reitz, J. R. Electronic Band Structure of Selenium and Tellurium. *Phys. Rev.* **1957**, *105*, 1233−1240.
(28) Liu, A.; Kim, Y.-S.; Kim, M. G.; Reo, Y.; Zou, T.; Choi, T.; Bai, S.; Zhu, H.; Noh, Y.-Y. Selenium Alloyed Tellurium Oxide for Amorphous p-Channel Transistors. *Nature* **2024**, *629*, 798−802.
(29) Zhang, Z.; Yang, X.; Liu, K.; Wang, R. Epitaxy of 2D Materials Toward Single Crystals. *Adv. Sci.* **2022**, *9*, No. 2105201, DOI: 10.1002/advs.202105201.
(30) Ji, J.; Song, X.; Liu, J.; Yan, Z.; Huo, C.; Zhang, S.; Su, M.; Liao, L.; Wang, W.; Ni, Z.; Hao, Y.; Zeng, H. Two-Dimensional Antimonene Single Crystals Grown by van der Waals Epitaxy. *Nat. Commun.* **2016**, *7*, No. 13352, DOI: 10.1038/ncomms13352.
(31) Hawley, C. J.; Beatty, B. R.; Chen, G.; Spanier, J. E. Shape-Controlled Vapor-Transport Growth of Tellurium Nanowires. *Cryst. Growth Des.* **2012**, *12*, 2789−2793.
(32) Koma, A.; Sunouchi, K.; Miyajima, T. Fabrication and Characterization of Heterostructures with Subnanometer Thickness. *Microelectron. Eng.* **1984**, *2*, 129−136.
(33) Nielsen, R.; Youngman, T. H.; Crovetto, A.; Hansen, O.; Chorkendorff, I.; Vesborg, P. C. K. Selenium Thin-Film Solar Cells with Cadmium Sulfide As a Heterojunction Partner. *ACS Appl. Energy Mater.* **2021**, *4*, 10697−10702.
(34) Hadar, I.; Hu, X.; Luo, Z.-Z.; Dravid, V. P.; Kanatzidis, M. G. Nonlinear Band Gap Tunability in Selenium-Tellurium Alloys and Its Utilization in Solar Cells. *ACS Energy Lett.* **2019**, *4*, 2137−2143.
(35) Qin, J.; Qiu, G.; Jian, J.; Zhou, H.; Yang, L.; Charnas, A.; Zemlyanov, D. Y.; Xu, C.-Y.; Xu, X.; Wu, W.; Wang, H.; Ye, P. D. Controlled Growth of a Large-Size 2D Selenium Nanosheet and Its Electronic and Optoelectronic Applications. *ACS Nano* **2017**, *11*, 10222−10229.
(36) Luo, L.-B.; Yang, X.-B.; Liang, F.-X.; Jie, J.-S.; Li, Q.; Zhu, Z.-F.; Wu, C.-Y.; Yu, Y.-Q.; Wang, L. Transparent and Flexible Selenium Nanobelt-Based Visible Light Photodetector. *CrystEngComm* **2012**, *14*, 1942−1947.
(37) Wang, Q.; Safdar, M.; Xu, K.; Mirza, M.; Wang, Z.; He, J. Van der Waals Epitaxy and Photoresponse of Hexagonal Tellurium Nanoplates on Flexible Mica Sheets. *ACS Nano* **2014**, *8*, 7497−7505.
(38) Hu, D.; Ye, C.; Wang, X.; Zhao, X.; Kang, L.; Liu, J.; Duan, R.; Cao, X.; He, Y.; Hu, J.; Li, S.; Zeng, Q.; Deng, Y.; Yin, P.-F.; Ariando, A.; Huang, Y.; Zhang, H.; Wang, X. R.; Liu, Z. Chemical Vapor Deposition of Superconducting $FeTe_{1-x}Se_x$ Nanosheets. *Nano Lett.* **2021**, *21*, 5338−5344.
(39) Shenasa, M.; Sainkar, S.; Lichtman, D. XPS Study of Some Selected Selenium Compounds. *J. Electron Spectrosc. Relat. Phenom.* **1986**, *40*, 329−337.
(40) Recatala-Gomez, J.; Kumar, P.; Suwardi, A.; Abutaha, A.; Nandhakumar, I.; Hippalgaonkar, K. Direct Measurement of the Thermoelectric Properties of Electrochemically Deposited Bi_2Te_3 Thin Films. *Sci. Rep.* **2020**, *10*, No. 17922, DOI: 10.1038/s41598-020-74887-z.
(41) Reese, M. O.; Perkins, C. L.; Burst, J. M.; Farrell, S.; Barnes, T. M.; Johnston, S. W.; Kuciauskas, D.; Gessert, T. A.; Metzger, W. K. Intrinsic Surface Passivation of CdTe. *J. Appl. Phys.* **2015**, *118*, No. 155305, DOI: 10.1063/1.4933186.
(42) Wei, X.; Wang, S.; Zhang, N.; Li, Y.; Tang, Y.; Jing, H.; Lu, J.; Xu, Z.; Xu, H. Single-Orientation Epitaxy of Quasi-1D Tellurium Nanowires on M-Plane Sapphire for Highly Uniform Polarization Sensitive Short-Wave Infrared Photodetection. *Adv. Funct. Mater.* **2023**, *33*, No. 2300141, DOI: 10.1002/adfm.202300141.
(43) Fu, L.; He, Y.; Zheng, J.; Hu, Y.; Xue, J.; Li, S.; Ge, C.; Yang, X.; Peng, M.; Li, K.; Zeng, X.; Wei, J.; Xue, D.-j.; Song, H.; Chen, C.; Tang, J. Te_xSe_{1-x} Photodiode Shortwave Infrared Detection and Imaging. *Adv. Mater.* **2023**, *35*, No. 2211522, DOI: 10.1002/adma.202211522.
(44) Liao, J.; Zhao, Y.; Hu, Z.; Bu, S.; Lu, Q.; Shang, M.; Jia, K.; Qiu, X.; Xie, Q.; Lin, L.; Liu, Z. Crack-Free Transfer of Graphene Wafers via Photoresist As Transfer Medium. *Acta Phys. -Chim. Sin.* **2023**, *39*, No. 2306038, DOI: 10.3866/PKU.WHXB202306038.
(45) Qin, B.; Ma, H.; Hossain, M.; Zhong, M.; Xia, Q.; Li, B.; Duan, X. Substrates in the Synthesis of Two-Dimensional Materials via Chemical Vapor Deposition. *Chem. Mater.* **2020**, *32*, 10321−10347.
(46) Li, R.; Yao, F.; Xu, Y.; Bai, S.; Jia, Z.; Lin, Q. Optimizing the Charge Carrier Dynamics of Thermal Evaporated Te_xSe_{1-x} Films for High-Performance Short-Wavelength Infrared Photodetection. *Adv. Funct. Mater.* **2024**, *34*, No. 2307005, DOI: 10.1002/adfm.202307005.
(47) Wang, Y.; Kim, J. C.; Wu, R. J.; Martinez, J.; Song, X.; Yang, J.; Zhao, F.; Mkhoyan, A.; Jeong, H. Y.; Chhowalla, M. Van der Waals Contacts between Three-Dimensional Metals and Two-Dimensional Semiconductors. *Nature* **2019**, *568*, 70−74.
(48) Wang, J.; Yao, Q.; Huang, C.-W.; Zou, X.; Liao, L.; Chen, S.; Fan, Z.; Zhang, K.; Wu, W.; Xiao, X.; Jiang, C.; Wu, W.-W. High Mobility MoS_2 Transistor with Low Schottky Barrier Contact by Using Atomic Thick h-BN As a Tunneling Layer. *Adv. Mater.* **2016**, *28*, 8302−8308.
(49) Liu, H.; Neal, A. T.; Zhu, Z.; Luo, Z.; Xu, X.; Tománek, D.; Ye, P. D. Phosphorene: An Unexplored 2D Semiconductor with a High Hole Mobility. *ACS Nano* **2014**, *8* (4), 4033−4041.

(50) Yang, S.-J.; Choi, M.-Y.; Kim, C.-J. Engineering Grain Boundaries in Two-Dimensional Electronic Materials. *Adv. Mater.* **2023**, *35*, No. 2203425, DOI: 10.1002/adma.202203425.
(51) Zhong, M.; Xia, Q.; Pan, L.; Liu, Y.; Chen, Y.; Deng, H.-X.; Li, J.; Wei, Z. Thickness-Dependent Carrier Transport Characteristics of a New 2D Elemental Semiconductor: Black Arsenic. *Adv. Funct. Mater.* **2018**, *28*, No. 1802581, DOI: 10.1002/adfm.201802581.
(52) Sun, H.; Zhou, X.; Wang, X.; Xu, L.; Zhang, J.; Jiang, K.; Shang, L.; Hu, Z.; Chu, J. P-N Conversion of Charge Carrier Types and High Photoresponsive Performance of Composition Modulated Ternary Alloy $W(S_xSe_{1-x})_2$ Field-Effect Transistors. *Nanoscale* **2020**, *12*, 15304−15317.
(53) Leong, W. S.; Li, Y.; Luo, X.; Nai, C. T.; Quek, S. Y.; Thong, J. T. L. Tuning the Threshold Voltage of MoS_2 Field-Effect Transistors via Surface Treatment. *Nanoscale* **2015**, *7*, 10823−10831.
(54) Zhang, X.; Liao, Q.; Liu, S.; Kang, Z.; Zhang, Z.; Du, J.; Li, F.; Zhang, S.; Xiao, J.; Liu, B.; Ou, Y.; Liu, X.; Gu, L.; Zhang, Y. Poly(4-styrenesulfonate)-Induced Sulfur Vacancy Self-Healing Strategy for Monolayer MoS_2 Homojunction Photodiode. *Nat. Commun.* **2017**, *8*, No. 15881, DOI: 10.1038/ncomms15881.
(55) Xia, Y.; Li, G.; Jiang, B.; Yang, Z.; Liu, X.; Xiao, X.; Flandre, D.; Wang, C.; Liu, Y.; Liao, L. Exploring and Suppressing the Kink Effect of Black Phosphorus Field-Effect Transistors Operating in the Saturation Regime. *Nanoscale* **2019**, *11*, 10420−10428.

https://doi.org/10.1021/acsnano.4c05323
ACS Nano 2024, 18, 17293−17303